IET Image Processing

Research Article

IET Journals
The Institution of Engineering and Technology

Automated glaucoma detection using retinal layers segmentation and optic cup-to-disc ratio in optical coherence tomography images

ISSN 1751-9659
Received on 15th May 2018
Revised 8th August 2018
Accepted on 24th September 2018
E-First on 17th December 2018
doi: 10.1049/iet-ipr.2018.5396
www.ietdl.org

Aneeqa Ramzan[1] ✉, Muhammad Usman Akram[1], Arslan Shaukat[1], Sajid Gul Khawaja[1], Ubaid Ullah Yasin[2], Wasi Haider Butt[1]

[1]*Computer Engineering Department, National University of Sciences and Technology, Islamabad, Pakistan*
[2]*Armed Force Institute of Ophthalmology, Rawalpindi, Pakistan*
✉ *E-mail: aneeqa_ramzan@yahoo.com*

Abstract: Glaucoma is a blindness causing eye disease if not treated in time and caused by the increase in the cup-to-disc region (CDR). A novel method for extraction of the inner limiting membrane (ILM) and retinal pigment epithelium (RPE) layers from optical coherence tomography scans is proposed. A new colour channels mean based quality assessment step is applied to segment out ILM layer for different quality images. During RPE segmentation, a new 'centroid based thresholding' method is proposed to remove extended ILM regions. The method uses both the ILM layer and RPE breakpoints for a cup and disc calculation, respectively. A novel criterion for horizontal/flat cup diameter based on the average RPE break points is proposed. Based on calculated CDRs, the system classifies the subject as normal or glaucomatous. The average sensitivity, accuracy, and specificity of the proposed system are 87, 79 and 72%, respectively, on the Armed Forces Institute of Ophthalmology dataset when correlated with clinical annotations and CDR computer generated values. The proposed system has shown the higher correlated result of 92.59% sensitivity with the senior most ophthalmologists. It promotes the e-health field at the retinal level and employed as the decision support system by the young doctors.

1 Introduction

Diagnostic medical imaging modality or computer-aided diagnosis (CAD) is a non-invasive practice that gives an insight of different parts of the body in order to support the diagnosis, detection, and treatment of diseases. Medical imaging and diagnostic radiology plays a vital role in public health worldwide and has become one of the major research topics in recent years [1]. These are established with diverse and complex characteristics as compared to each other for instance the optical coherence tomography (OCT), the fundus photography, the X-ray computed-tomography (CT) image, the magnetic-resonance imaging (MRI), the positron-emission tomography image, the digital-mammography, the ultrasound image, the dermoscopy image, the computed-radiography image etc., are associated with the hospital information and used widely in the clinical diagnosis [2, 3].

Glaucoma is an eye problem that affects the retina and leads to permanent blindness if not treated in initial stages. World Health Organisation has declared glaucoma to be the second largest cause of blindness all over the world [4]. Research done in 2014 declared 64.3 million glaucomatic patients worldwide in the year 2013 [5]. These numbers are set to increase to 80 million by 2020 [6] and to 111.8 million by 2040 [5]. Statistics reveal that the Asian countries such as Pakistan, India, China etc. has nearly ½ of the total glaucoma patients in the world. The reason behind this enormous prevalence of glaucoma, mostly primary-angle closure-glaucoma among Asians is due to their anatomically narrower angle between iris and sclera and trabecular meshwork clogs preventing normal outflow of aqueous humour from the eye [7]. They also reveal that not only doctor to patient ratio is extremely low and a shortage of trained people, but also resources to deploy modern imaging instruments. A number of patients lose their vision due to lack of information or unavailability of treatment. Self-diagnostic software for retinal diseases can help in the development of a tele-screening system to provide easy to access and cost effective solution. Any research in this situation can prove to be pretty useful at the national level.

Many computer-aided diagnostics are being proposed to analyse the OCT image and helps in the detection of many eye diseases. The proposed computer-aided diagnostic systems aids in screening out glaucoma cases. For glaucoma diagnosis, cup-to-disc region (CDR) is the main factor to classify glaucoma patients and is calculated by two commonly used imaging modalities, i.e. OCT and fundus imaging. Over the past few years, some CAD systems are being designed for glaucoma detection using fundus imaging modality to aid ophthalmologists by calculating CDR in glaucoma images. However, these diagnostic methods do not provide 100% accuracy due to lack of capability to screen all the glaucoma suspects, since fundus 2D imaging show structural changes due to glaucoma not in initial stages. So in this research, a 3D imaging technique, i.e. OCT is used to compute this incremented CDR known as cupping in glaucomatic patients. Previous work was mainly focused on the 2D analysis of retina but now the proposed algorithm uses the 3D analysis of retina, i.e. OCT imaging technique, which can facilitate in accurate retinal diseases diagnosis and retinal recognition. This would assist the ophthalmologists in detecting the ocular diseases and treating the patients in appropriate ways. Figs. 1*a* and *b* show normal and glaucomatous OCT scan, respectively, and Fig. 1*c* shows annotated OCT scan displaying inner limiting membrane (ILM) and retinal pigment epithelium (RPE) layers, which are extracted and analysed for the calculation of CDR from OCT images.

The detection and diagnosis of retinal diseases can be problematic. Increase in eye's internal intraocular pressure (IOP), age, medical and family history, medical conditions, and region-wise prevalence etc. are the risk-factors of glaucoma. Glaucoma detection can be done using perimetry, tonometry, gonioscopy, ophthalmoscopy, fundoscopy and the most effective optical-coherence-tomography. Therefore, we have proposed an automated computer-aided algorithm, which takes the OCT image as an input and correctly segments ILM and RPE layers, and CDR computation, i.e. fundamentals of glaucoma diagnosis. ILM layers in all images have already been annotated with the help of ophthalmologist. For more accurate disease detection and to check the reliability of the proposed system, the extracted CDR results from OCT are correlated with annotated CDRs by an expert ophthalmologist and with computer-CDR generated values

(CCGV). The rest of the paper is structured in the following manner. Section 2 defines state-of-art methods used by other researchers in the literature for glaucoma detection using multiple methods including retinal-layers segmentation and CDR computation in OCT. The proposed method for the optic cup to disc calculation based on ILM-layer and RPE-layer segmentation using OCT scans is presented in Section 3. Results are explained in Section 4. Discussion and conclusion are presented in Sections 5 and 6.

2 Literature review

Imaging modalities such as OCT, ultrasound, X-rays, CT scan, MRI etc. are used in bio-medical applications to visualise the human body's internal structure. The proposed methodology and results' reliability are evaluated when calculated parameters are correlated with clinical results suggested by an ophthalmologist. The calculation of CDR for glaucoma diagnosis is done using two imaging modalities, i.e. OCT and fundus imaging [8]. Earlier treatment of ocular diseases was carried out using progressive OCT imaging technologies based tools by means of monitoring/identifying the cross-sectional view of retinal tissue as displayed in Fig. 2. OCT provides the cross-sectional view of the retina and its axial resolution is around 1–15 µm which is 10–100 times better than ultrasound or MRI in order to cure eye diseases [9]. Spatial domain OCT (SD-OCT) imaging is widely employed in the enhancement of retinal evaluation measurements [10].

2.1 Clinical perspective of glaucoma diagnosis

Glaucoma is clinically identified and diagnosed by various researchers using OCT imaging technology. OCT parameters the such as ganglion cell layer (GCL) and optical nerve head (ONH) were measured to separate normal from glaucomatous eyes. Furthermore, both macula and ONH are considered for the same purpose. Patricia Hrynchak *et al.* compared estimated CDR measurement by considering 20 subjects using both OCT ONH and fundus images in [11] and concluded that CDR is accurately measured by OCT ONH images in normal subjects. Macula an oval-shaped retina's portion covers 5500 microns, with the midpoint at the fovea and is responsible for focused vision. Its disorders lead to macular diseases that outcome in vision loss [12]. Nathan M. Radcliffe *et al.* evaluated retinal nerve fibre layer (RNFL) thinning using SD-OCT to detect the changes and loss of 30% portion of the macula, i.e. retinal ganglion cells occur in early glaucoma, suspects or glaucoma progression They also determined that macular thickness can give better results than RNFL estimation [13]. Ji-Woong Lee *et al.* applied SD-OCT and visual field (VF) tests to find structure-function connection in the macula and plotted macular ganglion cell (GC)/inner plexiform layer (IPL) thickness. They also measured the average mean deviation and concluded that limited VF tests for functional damage can be used in macula due to overlapping with SD-OCT results [14]. Gondal *et al.* considered 50 subjects for both normal and perimetry glaucoma diagnosed patient eyes to clinically estimate RNFL thickness parameters using stratus OCT and then concluded with a positive/negative predictive value and diagnostic accuracy [15]. Morgan *et al.* recommended IPL and radial galial (RG) cells or dendrites damage protection to recover vision at glaucoma early stage using high resolution and broad spectral OCT under 5 µm [16].

2.2 Automated glaucoma diagnosis

Rao *et al.* checked functional and structural glaucomatous diagnostic abilities with the help of specificity, sensitivity, area under curve (AUC) and by measuring GC IPL thickness at different macular regions using SD-OCT, respectively. They performed these tests on 61 glaucomatous and 46 control eyes and concluded that SD-OCT is better to measure GCLIP thickness [17]. Evaluation of macular structural changes was performed clinically in glaucomatous eyes by Argo *et al.* by examining 58 total eyes using SD-OCT. They obtained and compared thicknesses of the inner nuclear layer, GCL + nerve fibre layer (NFL), photoreceptor layer, NFL and RPE using glaucomatous B-scans with control eyes

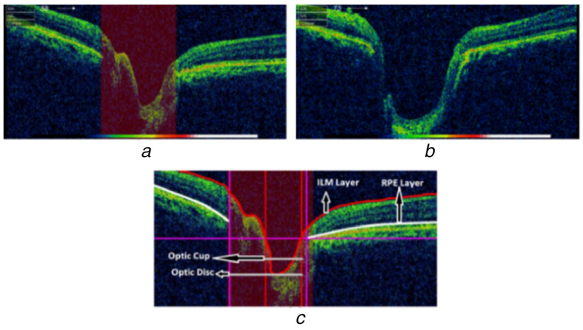

Fig. 1 *OCT scan with ILM and RPE layers in red and yellow, respectively, and cup and disc diameters in red and magenta, respectively (best viewed in colour online)*

(a) Normal OCT scan, ***(b)*** Glaucomatous OCT scan, ***(c)*** OCT scan with ILM and RPE layers in red and yellow, respectively, and cup and disc diameters in red and magenta, respectively

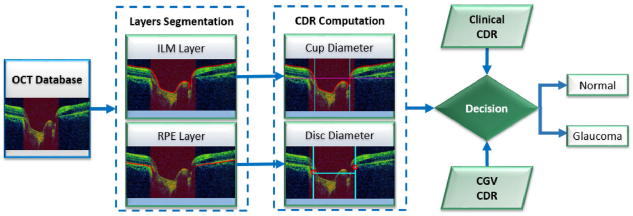

Fig. 2 *Block diagram for the proposed method*

group and then VF indices are correlated with retinal layer thickness using Spearman's rank test. They concluded that in glaucomatous eyes RPE and macular retinal layers are thinner [18]. Ahn *et al.* considered 103 open angle glaucomatous eyes and used RNFL/optic disc images and automated matched alternation flicker (AMAF) to measure the changes in RNFL thickness in order to detect functional and structural glaucoma progression. They draw a conclusion that one can get much improved results by AMAF than OCT and VF methods to visualise glaucoma progression and RNFL thickness degeneration's measurement [19]. In 2016, Stuart L. Graham *et al.* scanned RNFL to visualise ganglion cell complex (GCC) or GCL loss by considering 120 glaucomatous eyes in order to illustrate the increase in glaucoma detection capability with the help of these scans. They also compared OCT devices that are available commercially, i.e. Cirrus and Nidek to check their segmentation performance [20]. Naama Hammel *et al.* measured GCL, IPL, and GC IPL thicknesses in 181 glaucomatous and 57 healthy eyes to evaluate glaucoma progression by employing San Diego Automated-Layer Segmentation Algorithm and cubic thickness grid. They concluded that 68 years is the average age and the GCL and ganglion cell inner plexiform layer (GCIPL) rate variations are more rapid in glaucomatous eyes comparatively by using two macular scanning methods, i.e. systems, applications and products (SAP) and SD-OCT [21]. Pang *et al.* identified glaucoma in the retina using CDR in SD-OCT images by segmenting ILM and RPE using bilateral filtering and the OTSU thresholding method [22]. The automated glaucoma diagnosis method is proposed on a median filtered pre-processed OCT image by extracting features using discrete wavelet transform in the frequency domain. To classify the image as glaucoma or healthy, features are then selected using T-test class and are tested by support vector machine (SVM) classifier with radial basis function (RBF), multilayer perceptron (MLP), linear, quadratic and polynomial kernel functions [23]. A novel glaucoma diagnosis technique using OCT Angio (OCTA) images is introduced by estimating RNFL thickness and capillary density (CD) in order to categorise image as glaucoma or a normal one. They concluded that the CD and RNFL thickness values are observed to be lower in glaucoma patients than normal OCTA images in the glaucoma detection system [24]. Table 1 summarises the review from literature glaucoma detection using OCT images.

In the literature, most of the work is done from a clinical perspective but as far automated analysis of OCT images for

Table 1 OCT imaging for glaucoma diagnosis review

Year	Image modality	Features	Method	Dataset	Accuracy
2017	SD-OCT, VF tests	GC/IPL thickness [14]	GC/IPL thickness correlation	137 glaucoma eyes	—
2016	OCTA	RNFL thickness, CD [24]	—	local dataset: 49 normal, 18 glaucoma images	sensitivity 94%, specificity 91%
2015	OCT	CDR [8]	layer segmentation method	4 normal, 8 glaucoma images	accuracy 95%
2015	OCT	CDR, cup depth, retinal thickness [25]	—	OCT and fundus dataset: 50 normal, 100 glaucoma images	accuracy 93%
2015	OCT	wavelet coefficients [23]	discrete wavelet transform	200 glaucoma OCT images	accuracy 90%, specificity 89%, sensitivity 91%
2014	OCT	CDR, ILM [26]	range expansion based automated 3D graph-theoretic segmentation	10 glaucoma subjects	26–28% improvement
2013	OCT	CDR [22]	OTSU method for ILM and RPE	—	—
2012	OCT	CDR, ILM, RPE [22]	cup using ILM, disc using RPE break points	—	—
2011	OCT	RNFL thickness [15]	RNFL thickness	50 subjects	—
2010	3D-OCT	nine retinal layers [27]	gradient information and shortest path examination	19 glaucoma subjects	—

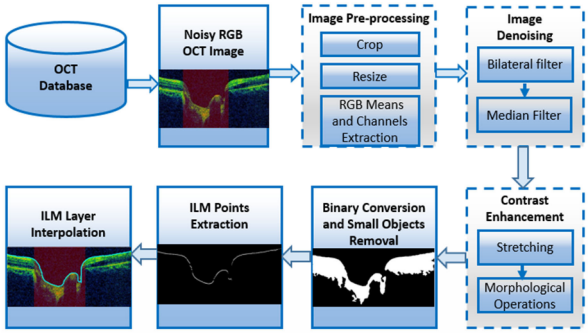

Fig. 3 *Block diagram for ILM extraction from OCT*

glaucoma detection is concerned, no significant work is found. The existing methods are a simple combination of basic image processing algorithms. The main reason for this is the unavailability of the standard OCT image dataset for glaucoma detection. OCT images are noisy in nature and retinal layers are also not properly visible for analysis, which make it a challenging task. In the proposed method, we have catered the issue of poor resolution and also reliable extraction of layers for glaucoma detection.

The major contributions made in this research are (i) collection of OCT database for analysis of glaucoma. This dataset is annotated by 04 ophthalmologists and will be made publicly available in our research group website (http://biomisa.org/index.php/downloads/). (ii) A new quality assessment criterion is proposed for the automated analysis of the OCT image without throwing away noisy samples. (iii) A hybrid filtering approach is introduced for enhancement of layers before extraction. (iv) A simple and time efficient, yet reliable interpolation technique is used for layer segmentation.

3 Proposed method

The proposed technique uses B-scans of optic nerve head centred SD-OCT images. The main goal of this research is to compute the cup-to-disc ratio to separate glaucoma from normal images. In SD-OCT, the internal retinal layers have been analysed to capture changes introduced by glaucoma. First of all, some specific layers are segmented from all OCT images. Layers required for CDR calculation are the top most and the bottom most layer of the retina, i.e. ILM and RPE, respectively, as these two layers are mostly used in the literature for CDR calculation and glaucoma detection. The horizontal cup diameter and horizontal disc diameter have been calculated by identifying cup and disc boundaries using segmented ILM and RPE layers. The horizontal CDR is then computed and then the subject is labelled as normal or diseased (glaucomatous). A fused decision-making system is being established in the proposed system. This system combines the CDR value for each image of three diverse systems, i.e. computed CDR (CCDR) from the OCT using the proposed method, CCGV and CDR values annotated by four expert ophthalmologists. The key focus is to analyse OCT, which is extremely sophisticated and the most recent method to evaluate glaucoma. The block diagram of the proposed method for glaucoma diagnosis is shown in Fig. 2.

3.1 Automated ILM segmentation in OCT retinal images for glaucoma detection

An automated glaucoma diagnosis algorithm is being developed by analysing the ILM layer in SD-OCT images. The ILM layer is extracted and interpolated from the retinal SD-OCT scan to separate out diseased images, i.e. glaucomatous from normal ones on the basis of the ILM behaviour. The block diagram of the algorithm for ILM extraction is displayed in Fig. 3.

3.1.1 Image preprocessing: Pre-processing is done on original images in ILM layer segmentation's first step. Pre-processing encompasses two stages, i.e. the first one is image cropping and rescaling/resizing, and the second one is a quality assessment of each OCT image, followed by green channel extraction for further processing. Cropping is done in order to extract a region of interest (ROI) from the original image. ROI in our case will be equal retinal layers length on both sides of the cup, as cup lies in the centre of the image [28]. Cup location differs in each scan, so manual cropping is done. Each manually cropped version is then rescaled to the size of its original image, i.e. 456 rows and 951 columns. The rescaling or resizing step is done to correctly classify the images after normalising them on the common resolution [29]. Bilinear-interpolation transformation is being used for image resizing in (1) [30]. In bilinear interpolation, four neighbour pixels are used to find one new unknown pixel, and $N = 1$ is kept to satisfy this condition

$$f(x, y) = \sum_{i=0}^{N} \sum_{j=0}^{N} a_{ij}\, x^i y^j; \quad N = 1, \tag{1}$$

where a_{ij} are intensity values, (x, y) are spatial locations and $f(x, y)$ is the interpolated pixel using bilinear interpolation.

Step 1 BEGIN
Step 2 Initialize counter $\boldsymbol{ILM_{thick}}$ to 80 (Counter to remove ILM thickness up to 80 pixels in each column)
Step 3 Make Binary Thresholded image of RPE $\boldsymbol{RPE_{img}}$
Step 4 Make ILM image $\boldsymbol{ILM_{img}}$ using interpolated ILM layer
Step 5 Make Black image $\boldsymbol{RILM_{img}}$ using interpolated ILM layer
Step 6 For each column in $\boldsymbol{ILM_{img}}$ (for $\boldsymbol{a = 1}$ to $\boldsymbol{c}$, where $\boldsymbol{c}$ is total columns of $\boldsymbol{ILM_{img}}$)
Step 7 For each row in $\boldsymbol{ILM_{img}}$ (for $\boldsymbol{b = 1}$ to $\boldsymbol{r}$, where $\boldsymbol{r}$ is total rows of $\boldsymbol{ILM_{imgR}}$)
Step 8 IF $\boldsymbol{ILM_{img}(\mathbf{b}, \mathbf{a}) == 1}$ THEN
Step 9 IF $\mathbf{b} + \boldsymbol{ILM\_thick} < \mathbf{r}$ THEN
- FOR each element till reach $\boldsymbol{ILM_{thick}}$ thickness value (for $\boldsymbol{i = 1}$ to $\boldsymbol{ILM_{thick}}$)
- Set $\mathbf{1} \leftarrow \boldsymbol{RILM_{img}}\ (\boldsymbol{b + i, a})$
- END FOR

Step 10 ELSE THEN
- Set $\mathbf{1} \leftarrow \boldsymbol{RILM_{img}}\ (\boldsymbol{b{:}r, a})$

Step 11 END IF ($\mathbf{b} + \boldsymbol{ILM\_thick} < \mathbf{r}$)
Step 12 END FOR (both FOR columns $\boldsymbol{a}$ and rows $\boldsymbol{b}$)
Step 13 Subtract $\boldsymbol{RPE_{img}}$ and $\boldsymbol{RILM_{img}}$ (to make new image having retained RPE portions)
Step 14 STOP

Fig. 4 *Algorithm 1: RPE portion retention*

All three channels, i.e. *R*, *G*, and *B* are being extracted from images. The OCT images normally have different qualities in terms of their noise. Some OCT images are too noisy for further processing, whereas others are comparatively less noisy. Variation is found in the behaviour of these two types of images when ILM is extracted. So, quality assessment of all OCT scans is performed on the basis of means computations of their three channels individually, as shown in Table 2. A pattern of the means in the red channel (mean *R*) and green channel (mean *G*) of each image is being observed for noisy images. Therefore, a check is applied to each image which separates out the noisy images. In the images with mean $R \leq 19$ and mean $G \geq 35.9$, nine out of total images are found noisy after this quality check. Means of blue channel (mean *B*) do not play any role in this assessment so have not been mentioned in the table. Two separate algorithms have been designed for very noisy (nine images), and less noisy (41 images). Further processing is done on the extracted green channel.

3.1.2 Image denoising: First, the existence of additive white Gaussian noise and speckle noise affects ILM layer segmentation and classification. So, the second step of the proposed method is to eliminate noise particles from OCT images using a novel approach which combines two step noise reduction methods. In the first step, all OCT scans are de-noised by bilateral and wiener filter in order to analyse filter's performance, it is being observed that the bilateral filter performed better than a wiener. So, further processing is carried out on bilateral resulting images. An accurate, fast-and-provable bilateral filter is selected due to its less computation time in comparison with other bilateral filters. Its complexity is cut down from O(*S*) to O (1) operations per pixel, where *S* denotes spatial-filter's support size. It performs nonlinear filtering while preserving edges with Gaussian as range kernel since edges play a vital role in correct ILM segmentation. Box-bilateral and Gaussian-bilateral are used to de-noise input green channel image separately. Then pixel by pixel addition of both box and Gaussian results is performed to enhance layers where they get

Table 2 Quality assessment on the basis of channels means

Quality assessment	Channel means	
	Mean red channel	Mean green channel
good quality images	36.625 ± 2.854	36.672 ± 3.337
bad quality images	15.258 ± 1.479	41.702 ± 3.225

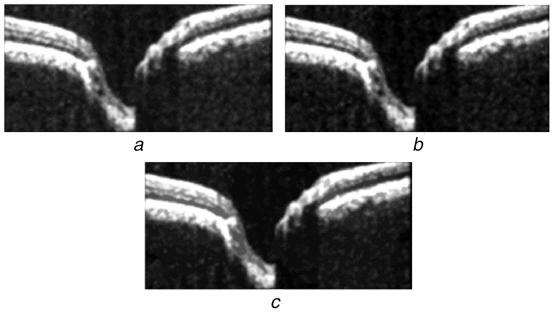

Fig. 5 *Image denoising and enhancement*
(a) Median filter applied on the added result of the bilateral box and bilateral Gaussian Enhanced Image, ***(b)*** Contrast stretching, ***(c)*** Morphological closing and holes filling

blurred during the bilateral process. The added result is much enhanced on layers portion and with very less noise in the resultant image. Equations (2)–(4) show bilateral filtering, bilateral-Gaussian filtering, and bilateral-box mathematically [31]

$$f_{\text{bilateral}}(i) = \frac{\left[\sum_{k \in \Omega_{\text{kernel}}} u(j) g_{\sigma_r}(f(i-j) - f(i)) f(i-j)\right]}{\left[\sum_{j \in \Omega_{\text{kernel}}} u(j) g_{\sigma_r}(f(i-j) - f(i))\right]}, \quad (2)$$

$$u(i) = \exp\left(-\frac{\|i\|^2}{2\sigma_{\text{s}}}\right), \quad i \text{ belongs to } \Omega_{\text{kernel}}, \quad (3)$$

$$u(i) = 1/|\Omega_{\text{kernel}}|, \quad (4)$$

where $f_{\text{bilateral}}(i)$ is the bilateral filter, $u(i)$ is the spatial-filter, Ω_{kernel} is the square-neighbourhood spatial kernel, σ is the standard deviation, σ_{r} is the range Gaussian width, σ_{s} is the Box kernel width and $\in$ is the kernel-approximation accuracy.

Both bilateral-box and bilateral-Gaussian filters use σ_{r} and $\in$ which are taken as 40 and 1×10^{-3} respectively. For box filter, σ_{s} is taken as 3. The second step further reduces any remaining speckle noise using a 2D-median filter. Algorithm 1 (see Fig. 4) uses 11×11 neighbourhoods, whereas algorithm 2 uses 5×5 neighbourhoods for nine and 41 images, respectively. Median filtering is shown in Fig. 5*a*.

3.1.3 Contrast enhancement: Contrast enhancement is being performed on the median resultant image. The enhanced and improved image is achieved after contrast-stretching and morphological-operations are used in combination as shown in Fig. 5. Normalisation or contrast-stretching linearly maps input, i.e. filter values to output values by increasing the dynamic range in the whole OCT median resultant image grey values as shown in Fig. 5*b* [32], morphological closing with a ball of radius 5 and height 1 of structuring element, and then holes filling is applied on the stretched image to achieve the desired results. Closing and filled holes results are displayed in Fig. 5*c* [33, 34].

3.1.4 Image thresholding and objects removal: The enhanced and de-noised grey scale version of each SD-OCT image is obtained once the contrast enhancement step is completed. Intensity based thresholding is now applied in order to extract and analyse the ILM layer. The performance of different thresholding values is checked empirically based on the top most layer where no information is being missed during binary conversion and gives the best ILM. The thresholding value is selected empirically after performance check. Therefore, $T = 0.275$ and 0.225 is applied on a

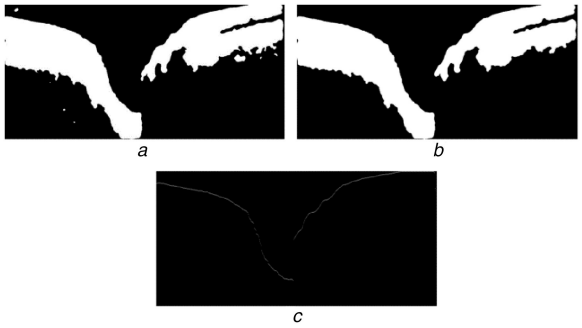

Fig. 6 *Thresholding and ILM Extraction*
(a) Binary conversion for both algorithms, ***(b)*** After removal of objects <500 pixels area, ***(c)*** Extracted ILM displayed in white

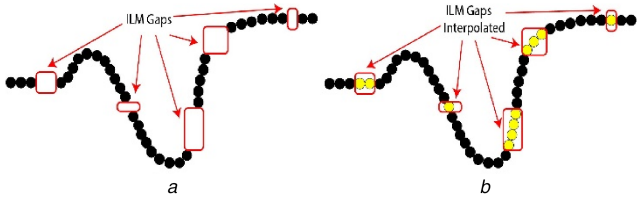

Fig. 7 *Linear interpolated example (best viewed in colour online)*
(a) With gaps, ***(b)*** Gaps filled after interpolation

set of ten images for the first algorithm, and on 41 images for the second algorithm, respectively. A binary converted OCT image is shown in Fig. 6*a*. Small bits and pieces of numerous sizes have been observed in the resulting images of thresholding. Therefore, in addition to thresholding, objects having <500 pixels area for both algorithms are also removed using connected component properties as shown in Fig. 6*b*. Connected component properties use the pixel ID list and area properties of image connected components in order to remove the specified area [35].

3.1.5 Image layer surface segmentation: CDR evaluation must be accurate for correct glaucoma diagnosis, therefore the extraction of the ILM layer plays the most vital part in cup diameter calculation. Thus, the extracted ILM layer's accuracy directly affects cup diameter's accuracy. As defined earlier, ILM is the top most retinal layer in the SD-OCT scan, so the first non-zero or white pixels are being picked to segment its surface. The resulting images after the object removal of 456 × 951 dimensions contain ones and zeros. ILM extracted images result in a 1D array of ones having 951 × 1 dimensions shown by ILM(Y) in (5) and Fig. 6*c*

$$\mathrm{ILM}(Y) = \sum_{\mathrm{col}=1}^{951} \left[\sum_{\mathrm{row}=1}^{456} \left(\mathrm{find}\left(\mathrm{in}_{\mathrm{img}}(\mathrm{row}, \mathrm{col}) = 1 \right) \right) \right], \tag{5}$$

where 'find' is finding the first non-zero pixel and $\mathrm{in}_{\mathrm{img}}$ is the input image of 456 rows and 951 columns.

3.1.6 ILM interpolation process: To fill the missing points or gap in the extracted ILM layer, interpolation is needed. Linear or nonlinear interpolation can be done using slope equation, second-order curve fitting, ellipse fitting or circular fitting methods. We did not use the existing interpolation methods but implemented the slope-line equation to interpolate the ILM layer, as the ILM layer is just a 1D array of zeros and ones. Mathematically shown by (6) and (7), the interpolated pixel output using two neighbouring pixels is shown by y, m represents slope, and C is a constant

$$y = mx + C, \tag{6}$$

$$m = (y1 - y0)/(x1 - x0)\,, \tag{7}$$

where $y \in (y0, y1)$ and $x \in (x0, x1)$.

Figs. 7*a* and *b* show a linear interpolation example before and after interpolating gaps using the proposed algorithm. Black dots

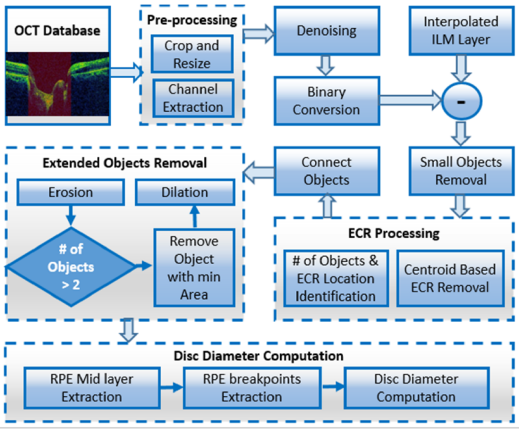

Fig. 8 *Block diagram for RPE extraction from OCT*

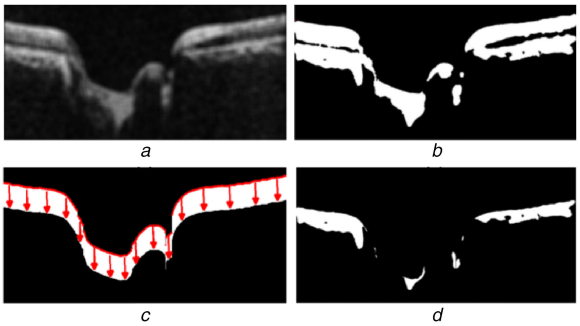

Fig. 9 *Image thresholding and RPE portion retention (best viewed in colour online)*
(a) De-noised using bilateral box filter, ***(b)*** Image thresholding result, ***(c)*** 80 pixels downwards in each column from top ILM layer extension shown by red arrows, ***(d)*** Subtracted resultant image of 'b' and 'c' shows retained RPE portion

are the extracted points of the ILM layer during the segmentation process. Red boxes show the gaps before interpolation in both Figs. 7*a* and *b*. Yellow dots in Fig. 7*b* show filled or interpolated gaps after the proposed algorithm, i.e. line-slope equation.

3.2 Automated RPE segmentation in OCT retinal images for glaucoma detection

After successful segmentation of the ILM layer, an automated algorithm is being developed by analysing the RPE layer in SD-OCT images for glaucoma diagnosis. The RPE layer is extracted and disc computation based on the RPE layer is performed in the retinal OCT scan to differentiate diseased images from normal ones. This differentiation is done on the basis of the computed disc diameter and CDR value, where RPE breakpoints are used for disc computation in SD-OCT images. The block diagram of the algorithm for RPE extraction is displayed in Fig. 8.

3.2.1 Image pre-processing: In contrary to the ILM layer segmentation, RPE does not need the quality assessment step because the ILM layer is the top layer where speckle noise attachment to the layer during segmentation leads to incorrect results. However, as RPE is the bottom layer, speckle noise does not get attached to that. Therefore, RPE extraction in both poor- and high-quality images is done using the same parameters.

3.2.2 Image de-noising: Filter analysis is already been carried out in the ILM de-noising step and the fast-and-provable bilateral filter was considered best for such a noise. During RPE segmentation, a novel approach is used which uses a bilateral box filter to eliminate noise in order to retain the significant features of the retinal OCT image. Fig. 9*a* shows a noise free image result. The bilateral-box filter uses σ_s which is taken as three in this case.

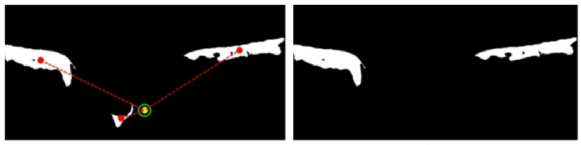

Fig. 10 *ECR processing using centroid-based thresholding (best viewed in colour online)*

(a) Centroid-based thresholding: centroids of objects using red dots, ECR location using yellow circle outlined by a green circle, distances by red dotted lines, ***(b)*** Resultant image after centroid-based thresholding

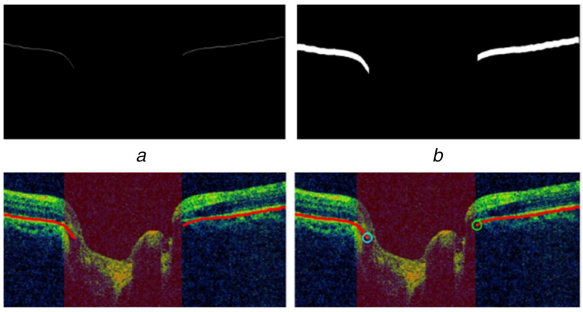

Fig. 11 *RPE flattening and segmentation (best viewed in colour online)*

(a) Object top ON pixels, ***(b)*** Flattened objects: extended ON pixels to 20 pixels in each column in downwards direction, ***(c)*** RPE central layer extraction, ***(d)*** RPE break points extraction

3.2.3 Image thresholding and RPE portion retention: Image thresholding is performed on the bilateral box noise-free resultant image. Binary or monochrome conversion is done using the OTSU thresholding method with a grey level histogram, which finds and sets a specific threshold value for each image. The threshold value is set by minimising the weighted within-class variance. The algorithm used for RPE portion retention is as follows:

Fig. 9*b* shows the binary image after OTSU thresholding, Fig. 9*c* shows white pixels extended to 80 pixels width in vertical downwards direction in each column displayed by red arrows and Fig. 9*d* shows a resultant image having retained RPE objects after subtraction of Figs. 9*b* and *c*.

3.2.4 Small objects removal: Numerous small bits and pieces are detected in the resultant image of retained RPE portion which acts as noise while segmenting the RPE layer. Therefore, the objects <500 area and 1000 pixels are removed from the resultant image. Small objects having <500 and 1000 pixels area for both algorithms are also removed using connected component properties and objects area in the binary image, respectively. Connected component properties use the pixel ID list and area properties of the image connected components in order to remove the specified area [35].

3.2.5 Extended cup region (ECR) processing using centroid-based thresholding: ECR is left even after small objects removal step, due to its larger area than the threshold pixel area value which is set for small objects. Sometimes, ECR size is similar to RPE objects, so they cannot be removed using small objects removal. ECR is the region which is in the bottom and centre of the image and is a part of the optic cup in retinal layers. To remove this ECR, first of all, centroids of all the objects are being identified and located displayed. Secondly, a novel approach named 'centroid-based thresholding' is being developed to get rid of ECR. According to this approach, the distance is being computed from the ECR point to all the centroids located in the first step. ECR is the point crossing the 100th row from the bottom and centre of the image shown by a yellow filled circle outlined by a green circle to make it prominent in Fig. 10*b*. Objects having computed centroid distance greater than the threshold value will be removed keeping RPE objects in the resultant image as displayed in Fig. 10*c*.

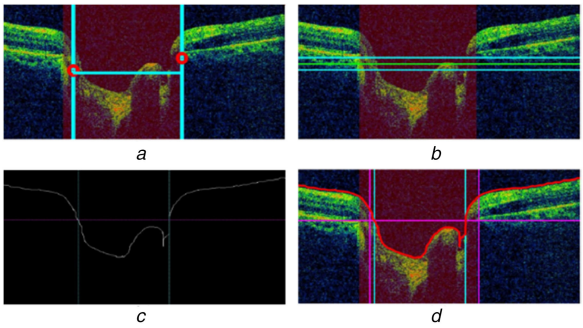

Fig. 12 *Disc and cup diameter computation (best viewed in colour online)*

(a) Horizontal disc diameter using red breakpoints in cyan, ***(b)*** Average of breakpoints in green horizontal line, ***(c)*** Horizontal cup diameter by vertical cyan lines, ***(d)*** Cup using cyan and disc using magenta

3.2.6 Connect detached objects: Some detachments are being observed in the objects that can lead to the inaccurate RPE central layer and breakpoints extraction. Thus, these detached objects with gaps need to be connected. Morphological dilation is used for the connection. A disc-shaped structuring element is used and the size of the disc will be increased until the gap is connected. This is done in order to make dilation generalised for any type of incoming OCT binary image. If the number of objects is greater than two, the gap will be connected.

3.2.7 RPE flattening and extended objects removal: The objects having RPE layers are uneven in nature and extraction of the RPE layer from this uneven image can be problematic. Before layer extraction, objects flattening are done for correct RPE segmentation. First of all, top ON/white pixels of RPE objects are picked as shown in Fig. 11*a*, and then they are extended to 20 pixels downwards in each column as shown in Fig. 11*b*. In some images, extended objects are being observed that needs to be removed. Extended objects removal is done by using the combination of morphological operations and connected component properties. First, the flattened image is eroded and then a decision check is applied on this eroded image. Decision based on a number of objects >2 is being established. If objects are >2, the object having a minimum area is removed using linear pixel indices. The image is again dilated to retain its original width. The same horizontal structuring element is used for both erosion and dilation.

3.2.8 RPE central layer and breakpoints extraction: The last step of RPE segmentation is to extract the RPE layer, i.e. the central layer after resultant flattening and extended objects removal. Average points are computed using top and bottom ON pixels of the objects as shown in red in Fig. 11*c*. These left and right RPE central layers are used to extract RPE break points which will be further used for disc diameter computation. The left break point is shown by cyan and right by the green circle in Fig. 11*d*.

3.3 Optic cup-to-disc computation

After successful ILM and RPE layers segmentation, optic cup and optic disc diameters are computed using ILM and RPE in SD-OCT images for glaucoma diagnosis.

3.3.1 Disc diameter computation: Disc diameter is computed using RPE layer break points. Fig. 12*a* shows disc diameter in cyan colour, where the red circle shows the breakpoints. Fig. 12*b* shows the average point of horizontal values of break points in green, where horizontal cyan colour is showing breakpoints. Equation (8) represents optic disc diameter mathematically, where $\mathrm{bp}_{\mathrm{verR}}$ is the right RPE break point and $\mathrm{bp}_{\mathrm{verL}}$ is the left RPE break point. Vertical coordinates are considered for horizontal disc diameter $\mathrm{disc}_{\mathrm{hor\_dia}}$ computation

$$\mathrm{disc}_{\mathrm{hor\_dia}} = \mathrm{bp}_{\mathrm{verR}} - \mathrm{bp}_{\mathrm{verL}}\,. \tag{8}$$

Table 3 Flat cup analysis

Image	Computed disc	Possible cup Using average clinical CDR
1	262	78.6
2	245	68.6
3	260	67.6
4	214	111.28
5	161	66.01
6	236	63.72
7	256	76.8
8	220	57.2
9	206	55.62

3.3.2 Cup diameter computation: Cup diameter is computed using the combined ILM and RPE layer. The average breakpoints crossing the ILM layer are the points of the cup and are shown in Fig. 12*c*. Fig. 12*d* shows the optic cup and optic disc on the original image. Equation (9) computes optic cup diameter $\text{cup}_{\text{hor\_dia}}$, where $\text{midbp}_{\text{verR}}$ is the right coordinate of the average RPE break points and $\text{midbp}_{\text{verL}}$ is the left coordinate of the average RPE break points.

$$\text{cup}_{\text{hor\_dia}} = \text{midbp}_{\text{verR}} - \text{midbp}_{\text{verL}}. \tag{9}$$

3.3.3 CDR computation: The optic-cup to optic-disc ratio is computed by taking the ratio of the horizontal cup diameter to horizontal disc diameter. Equation (10) shows the CDR ratio computation

$$\text{CDR}_{\text{ratio}} = \frac{\text{cup}_{\text{hor\_dia}}}{\text{disc}_{\text{hor\_dia}}}. \tag{10}$$

A threshold based binary classification is being performed based on the CDR values. Values >0.5 are considered glaucomatous, and <0.5 as normal [36]. Two labels, i.e. 'yes' and 'no' for a glaucomatous and normal eye, respectively, based on the 0.5 threshold value are then assigned to the CCDR of the proposed algorithm, CCGV, and clinical CDR values. After labels assigned to the whole dataset, confusion matrix, true positives (TPs), true negatives (TNs), false positives (FPs) and false negatives (FNs) are computed based on the classification of normal eyes from glaucomatous eyes in OCT imaging. In some cases, flat cups may be detected. Flat cups are those having no cup points identified between RPE break points' average horizontal line. In this case, cup = 0 with less or zero depth than typical cups, the resulting CDR value of <0.5 and hence declaring it as normal. Flat cup analysis is done on nine images when ILM is above mid-RPE breakpoints and results are shown in Table 3 for computing CDR. The possible cups are computed using already computed disc diameters, average clinical CDR and computed generated CDR values. It is observed that the possible computed cups using the average clinical CDR are close to the value of 65. Therefore, to cater to this issue of a flat cup a value of absolute 65 is assigned to the cup and CDR is computed.

4 Results

The proposed automated glaucoma diagnostic system is implemented in MATLAB 2014a. OCT imaging, being a state-of-the-art trend of detecting numerous ophthalmic diseases, is used for the detection of glaucoma. The proposed CAD system takes an OCT image as input and classifies it as glaucoma or healthy.

4.1 Dataset and annotations

The SD-OCT local dataset used for glaucoma analysis is obtained from the Armed Forces Institute of Ophthalmology (AFIO), Pakistan. A total of 50 optic nerve head centred OCT B-scan images with 456 × 951 resolution were acquired. Dataset has both right and left eye images of 25 subjects, i.e. 14 glaucomatous and 11 healthy. A TOPCON'S 3D OCT-1000 camera is used to acquire the OCT images. The cup-to-disc ratio of the CDR of the whole dataset is annotated by four expert ophthalmologists in order to evaluate the proposed algorithm performance. The system has also been analysed by comparing the CCDR values with CCGV. The CCGVs are automatically calculated during the OCT scan by built-in software. Table 4 shows both clinical and CCGV annotated CDRs. Means of channels, i.e. red channel mean and green channel mean are used as an evaluation parameter for the separation of high-quality images from low-quality images. For both quality images, different parameters are used in multiple steps performed for the proposed methodology. The ILM layers in all images have been annotated with the help of an ophthalmologist. Illustrator CS6 is used to draw ILMs manually pixel by pixel for all images. Figs. 13*a* and *b* show normal eye and its annotated ILMs, respectively, whereas Figs. 13*c* and *d* show glaucomatous eye using OCT and its annotated ILMs, respectively.

4.2 Experimentation

Evaluation and analysis of the proposed algorithm are done on multiple levels, i.e. ILM, CDR, and glaucoma. Both computation time and the pixel-wise comparison are made for ILM segmentation using the proposed system. Quantified errors are being computed by the pixel wise comparison of ophthalmologist-annotated ILMs with the proposed linear ILM results and Bezier curve fitting results. CDR from the proposed system is then correlated with the clinical and CGV-annotated CDRs and errors are calculated. Glaucoma and normal OCT images are then classified based on the CCDR values. A detailed analysis is given below.

4.2.1 ILM segmentation subjective and quantitative analysis: The proposed algorithm for ILM layer segmentation is tested on the whole dataset and both subjective and quantitative analyses are being done. Fig. 14*a* displays the pictorial results showing original images in the first top row, manually annotated ILMs in cyan in Fig. 14*b* and Bezier curve fitted results in green in Fig. 14*c*. Fig. 14*d* displays segmented ILM layers using the proposed linear interpolation method in red on OCT images. Fig. 14 also shows the zoomed versions of all three ILMs on cup locations, and it is being observed that the ILM extracted from the proposed system is highly correlated with the annotated ILM.

The Proposed algorithm segments the ILM layers from all 50 images. These quantified errors are calculated for all 50 images. Table 5 shows the mean quantified results by showing the pixel wise errors between manual annotation, Bezier curve and extracted ILM. The Euclidean distance is used to compute this quantified error. The quantitative results of 50 images showed that the proposed system has an error of mean Euclidean distance 7.08 ± 3.7 pixels and Bezier ILM layer with 6.85 ± 2.96 pixels, respectively, as compared to manual annotation. Bezier curve takes 9.83 s computation time, and the proposed algorithm for ILM interpolation takes 0.0087 s computation time for a single image as shown in Table 5.

This elapsed time shows that the proposed method is 1000 times computationally effective as compared to the Bezier curve.

Table 4 CDR annotations

Image	Clinical CDR and CGV CDR annotations					Image	Clinical CDR and CGV CDR annotations				
	Op 1 CDR	Op 2 CDR	Op 3 CDR	Op 4 CDR	CGV CDR		Op 1 CDR	Op 2 CDR	Op 3 CDR	Op 4 CDR	CGV CDR
1	0.3	0.3	0.4	0.3	0.46	26	0.3	0.1	0.2	0.4	0.43
2	0.3	0.35	0.4	0.5	0.43	27	0.3	0.1	0.3	0.3	0.34
3	0.6	0.7	0.7	0.75	0.66	28	0.4	0.3	0.4	0.5	0.48
4	0.5	0.4	0.6	0.7	0.56	29	0.4	0.55	0.5	0.6	0.52
5	0.8	0.75	0.8	0.7	0.71	30	0.5	0.5	0.5	0.5	0.42
6	0.3	0.2	0.4	0.5	0.5	31	0.4	0.7	0.9	0.7	0.47
7	0.3	0.1	0.3	0.2	0.3	32	0.3	0.7	0.9	0.65	0.43
8	0.3	0.1	0.2	0.2	0.39	33	0.9	0.8	0.9	0.9	0.8
9	0.3	0.4	0.4	0.4	0.41	34	0.3	0.4	0.5	0.4	0.57
10	0.3	0.35	0.3	0.4	0.37	35	0.5	0.6	0.7	0.7	0.53
11	0.6	0.8	0.8	0.7	0.53	36	0.4	0.45	0.5	0.5	0.58
12	0.5	0.6	0.7	0.7	0.47	37	0.6	0.65	0.6	0.8	0.58
13	0.3	0.3	0.5	0.5	0.45	38	0.6	0.7	0.7	0.8	0.59
14	0.5	0.4	0.5	0.45	0.5	39	0.8	0.3	0.4	0.4	0.73
15	0.6	0.6	0.7	0.7	0.55	40	0.4	0.2	0.4	0.4	0.4
16	0.5	0.7	0.7	0.7	0.56	41	0.3	0.1	0.7	0.3	0.65
17	0.3	0.2	0.3	0.4	0.3	42	0.7	0.2	0.5	0.3	0.56
18	0.8	0.2	0.4	0.3	0.74	43	0.6	0.6	0.7	0.7	0.64
19	0.5	0.5	0.7	0.6	0.51	44	0.5	0.7	0.7	0.75	0.65
20	0.6	0.65	0.9	0.6	0.64	45	0.2	0.2	0.2	0.3	0.45
21	0.3	0.3	0.6	0.2	0.4	46	0.3	0.2	0.3	0.3	0.4
22	0.5	0.45	0.4	0.5	0.45	47	0.6	0.65	0.6	0.7	0.65
23	0.4	0.45	0.5	0.6	0.55	48	0.65	0.7	0.6	0.7	0.74
24	0.3	0.3	0.3	0.4	0.41	49	0.3	0.3	0.3	0.2	0.23
25	0.8	0.8	0.9	0.9	0.7	50	0.2	0.3	0.4	0.25	0.23

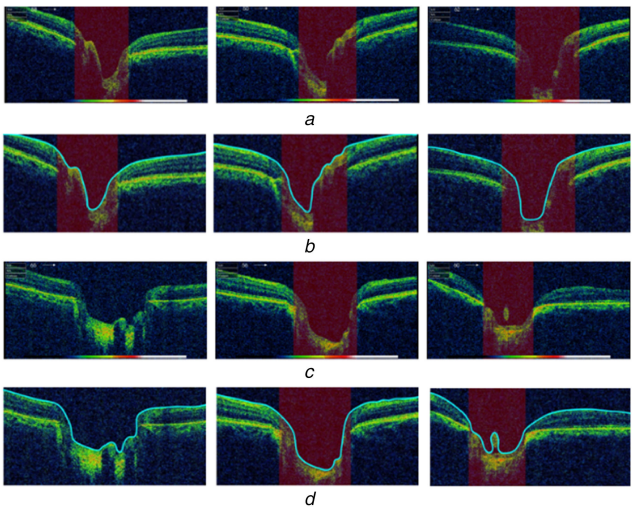

Fig. 13 *Healthy and Glaucomatous OCT Scans with and without ILM Annotations*
(a) Healthy OCT, ***(b)*** Annotated ILM on healthy OCT, ***(c)*** Glaucomatous OCT, ***(d)*** Annotated ILM on Glaucomatous OCT

Furthermore, the proposed method achieves better results than Bezier, as Bezier curve omits points during interpolation but the proposed method uses all points and is the simplest method for curve interpolation. These results show that there is no major difference in pixel wise error, but huge computation wise difference between the Bezier curve fit and the proposed interpolation method exists.

4.2.2 Cup-to-disc ratio quantitative analysis: The CCDR using the proposed algorithm is compared with CCGV and clinical values to check the reliability of our CAD system. For clinical correlation, OCT CCDR using our proposed methodology are compared with fundus CDR values annotated by four ophthalmologists are shown in Table 6. The CGV are automatically calculated during the OCT scan by built-in software. The proposed system performance has also been analysed by comparing the CDR values with CGV CDRs. The table also shows the computed mean error of CCDR with CGV CDR to be 0.143 ± 0.1, and with clinical CDR to be 0.1768 ± 0.12, 0.139 ± 0.1, 0.1178 ± 0.08, and 0.1116 ± 0.07. The difference of opinion is being observed between clinical CDRs. The expertise or seniority level increases from ophthalmologist 1 to 4, resulting ophthalmologist 4 the senior most among all with maximum experience. Annotated CDR of all four ophthalmologists is compared with CGV to analyse performance on the complete dataset. The proposed system provides a mean error on CGV CDR when compared with all annotated CDR on the whole 50 datasets to be 0.1197 ± 0.023. Taking the human error factor in consideration, our proposed system acts as a standard diagnostic system on which all doctors with different expertise level can rely upon and use it as a reliable system for young doctors. Our proposed system is created by mainly considering and matching diagnostic results with experienced doctors in order to use it as a reliable system for young doctors. Fig. 15 shows an error bar graph between the clinical CDRs on the whole dataset and CDR values calculated by the proposed system. The proposed system provides a mean error on CCDR when compared with all annotated CDR on the whole dataset to be 0.138 ± 0.026. Fig. 16 shows an error graph between the CGV CDRs on the whole dataset and CCDR values calculated by the proposed system.

4.2.3 CDR-based glaucoma classification: The labels are assigned to the CCDR of the proposed algorithm, CCGV, and clinical CDR values to classify normal eyes from glaucomatous eyes in OCT imaging. A threshold-based binary classification is being performed based on the CDR values. The CDR values ≥ 0.5 are assigned 'yes' label considering them glaucomatous, and <0.5 as normal and assigned a 'no' label [36]. Table 7 shows the confusion matrix of CCDRs as a predicted class and clinical CDRs as an actual class. In the same manner, Table 7(E) shows the confusion matrix of CCDRs as a predicted class and CGV CDRs as an actual class.

TPs and TN are the glaucomatous images identified as glaucomatous and normal images diagnosed as normal,

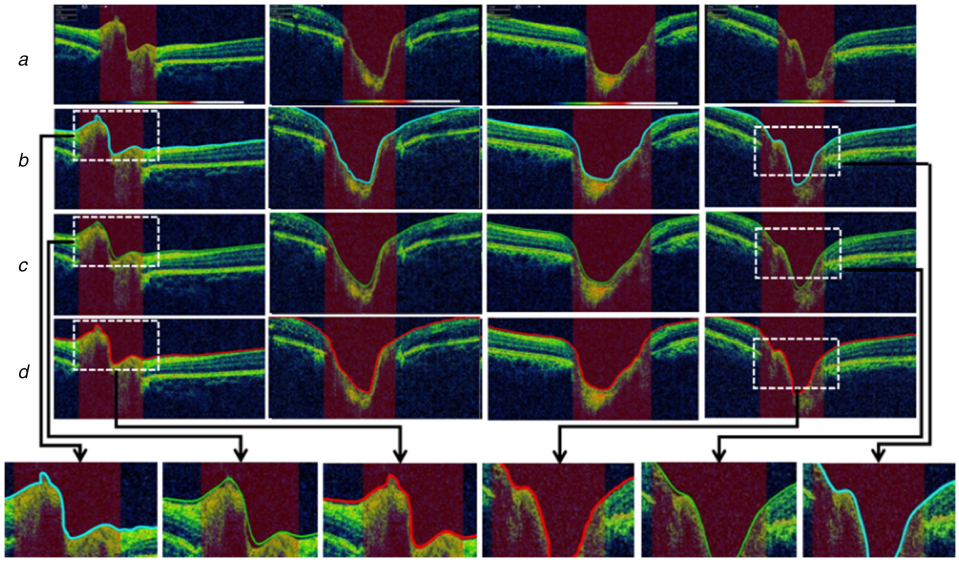

Fig. 14 *ILMs Comparison in OCT Scans*
(a) Original images, ***(b)*** Annotated ILM layers, ***(c)*** Bezier fit and manually annotated ILM plots, ***(d)*** Extracted ILM plots from our proposed algorithm

Table 5 Quantified errors of annotated ILM with the proposed method and Bezier curve fit and Elapsed time comparison of the proposed interpolation method with Bezier curve fitting

Interpolation method	Time of computation, s	Quantified mean Euclidean error with annotated ILM (pixels)	System specifications
Bezier curve fitting	9.83 s	6.85 ± 2.96 pixels	Intel®, core™ i3, CPU@1.7 GHz, RAM = 4 GB, 64 bit operating system, windows 8.1
proposed methodlinear interpolation	**0.0087 s**	7.08 ± 3.7 pixels	

Table 6 CCDR, clinical CDR and computer generated CDR correlation

Image	CCDR, clinical CDR and CGV CDR correlation						Image	CCDR, clinical CDR and CGV CDR correlation					
	CCDR	Op 1 CDR	Op 2 CDR	Op 3 CDR	Op 4 CDR	CGV CDR		CC DR	Op 1 CDR	Op 2 CDR	Op 3 CDR	Op 4 CDR	CGV CDR
1	0.46	0.3	0.3	0.4	0.3	0.46	26	0.26	0.3	0.1	0.2	0.4	0.43
2	0.46	0.3	0.35	0.4	0.5	0.43	27	0.25	0.3	0.1	0.3	0.3	0.34
3	0.55	0.6	0.7	0.7	0.75	0.66	28	0.6	0.4	0.3	0.4	0.5	0.48
4	0.54	0.5	0.4	0.6	0.7	0.56	29	0.72	0.4	0.55	0.5	0.6	0.52
5	0.65	0.8	0.75	0.8	0.7	0.71	30	0.66	0.5	0.5	0.5	0.5	0.42
6	0.55	0.3	0.2	0.4	0.5	0.5	31	0.64	0.4	0.7	0.9	0.7	0.47
7	0.38	0.3	0.1	0.3	0.2	0.3	32	0.69	0.3	0.7	0.9	0.65	0.43
8	0.45	0.3	0.1	0.2	0.2	0.39	33	0.63	0.9	0.8	0.9	0.9	0.8
9	0.48	0.3	0.4	0.4	0.4	0.41	34	0.51	0.3	0.4	0.5	0.4	0.57
10	0.49	0.3	0.35	0.3	0.4	0.37	35	0.57	0.5	0.6	0.7	0.7	0.53
11	0.8	0.6	0.8	0.8	0.7	0.53	36	0.79	0.4	0.45	0.5	0.5	0.58
12	0.84	0.5	0.6	0.7	0.7	0.47	37	0.82	0.6	0.65	0.6	0.8	0.58
13	0.51	0.3	0.3	0.5	0.5	0.45	38	0.85	0.6	0.7	0.7	0.8	0.59
14	0.41	0.5	0.4	0.5	0.45	0.5	39	0.3	0.8	0.3	0.4	0.4	0.73
15	0.73	0.6	0.6	0.7	0.7	0.55	40	0.64	0.4	0.2	0.4	0.4	0.4
16	0.74	0.5	0.7	0.7	0.7	0.56	41	0.4	0.3	0.1	0.7	0.3	0.65
17	0.24	0.3	0.2	0.3	0.4	0.3	42	0.42	0.7	0.2	0.5	0.3	0.56
18	0.23	0.8	0.2	0.4	0.3	0.74	43	0.71	0.6	0.6	0.7	0.7	0.64
19	0.69	0.5	0.5	0.7	0.6	0.51	44	0.68	0.5	0.7	0.7	0.75	0.65
20	0.86	0.6	0.65	0.9	0.6	0.64	45	0.27	0.2	0.2	0.2	0.3	0.45
21	0.4	0.3	0.3	0.6	0.2	0.4	46	0.25	0.3	0.2	0.3	0.3	0.4
22	0.62	0.5	0.45	0.4	0.5	0.45	47	0.59	0.6	0.65	0.6	0.7	0.65
23	0.48	0.4	0.45	0.5	0.6	0.55	48	0.52	0.65	0.7	0.6	0.7	0.74
24	0.45	0.3	0.3	0.3	0.4	0.41	49	0.29	0.3	0.3	0.3	0.2	0.23
25	0.71	0.8	0.8	0.9	0.9	0.7	50	0.31	0.2	0.3	0.4	0.25	0.23
							mean error CCDR		0.1768 ± 0.12	0.14 ± 0.1	0.12 ± 0.08	0.11 ± 0.07	0.14 ± 0.1

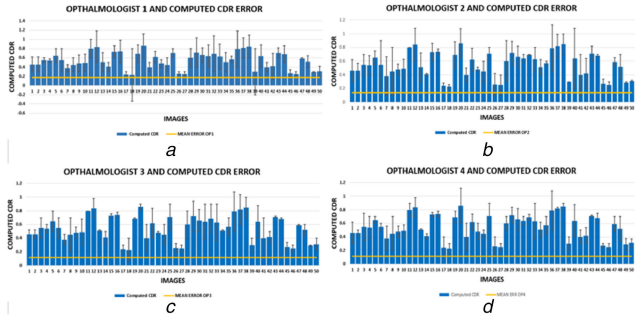

Fig. 15 *CCDR comparison with clinical CDR*

(a) Ophthalmologist 1, ***(b)*** Ophthalmologist 2, ***(c)*** Ophthalmologist 3, ***(d)*** Ophthalmologist 4

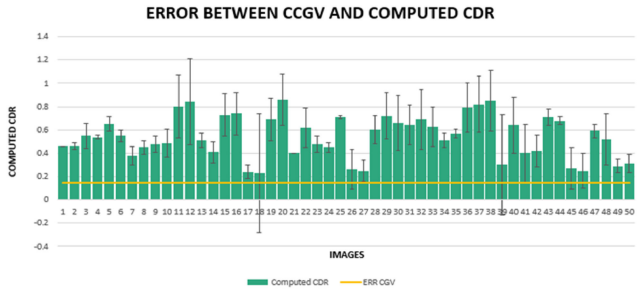

Fig. 16 *CCDR comparison with CGV CDR value*

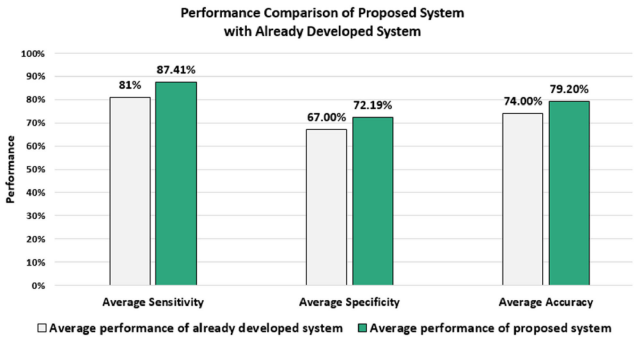

Fig. 17 *Performance comparison of the proposed system with an already developed system*

respectively, by the system. FPs and FNs are the normal images but diagnosed as glaucomatous and are the glaucomatous images but diagnosed as normal, respectively. Specificity and sensitivity give the accuracy of the system. Where accuracy, specificity, and sensitivity are defined mathematically in (11)–(13)

$$\text{Accuracy} = \frac{\text{TP} + \text{TN}}{\text{TP} + \text{TN} + \text{FP} + \text{FN}}, \tag{11}$$

$$\text{Specificity} = \frac{\text{TN}}{\text{TN} + \text{FP}}, \tag{12}$$

$$\text{Sensitivity} = \frac{\text{TP}}{\text{TP} + \text{FN}}. \tag{13}$$

Table 8 shows accuracy, sensitivity, and specificity when our proposed system is compared with CGV, and clinical systems [ophthalmologist 1, ophthalmologist 2, ophthalmologist 3, and ophthalmologist 4]. Tables 7(A) and 8 show the performance comparison of the CDR annotated by ophthalmologist 1 with the proposed system result by classifying 20 out of 24 glaucomatous cases correctly giving 83% sensitivity, 17 out of 26 normal cases correctly giving 65.38% specificity, and give 74% accuracy. A comparison result with ophthalmologist 2 classifies 19 out of 19 glaucomatous cases correctly giving 100% sensitivity, 21 out of 31 normal cases correctly giving 67.7% specificity, and give 80% accuracy as shown in Tables 7(B) and 8. A comparison result with

Table 7 CCDR of proposed system compared with clinical CDR results and computer generated CDRs

(A) Ophthalmologist 1 with Computed CDR

Confusion Matrix		Predicted Class: No / Healthy	Predicted Class: Yes/ Glaucoma
Actual Class	No / Healthy	17	9
	Yes/ Glaucoma	4	20

(B) Ophthalmologist 2 with Computed CDR

Confusion Matrix		Predicted Class: No / Healthy	Predicted Class: Yes/ Glaucoma
Actual Class	No / Healthy	21	10
	Yes/ Glaucoma	0	19

(C) Ophthalmologist 3 with Computed CDR

Confusion Matrix		Predicted Class: No / Healthy	Predicted Class: Yes/ Glaucoma
Actual Class	No / Healthy	16	4
	Yes/ Glaucoma	5	25

(D) Ophthalmologist 4 with Computed CDR

Confusion Matrix		Predicted Class: No / Healthy	Predicted Class: Yes/ Glaucoma
Actual Class	No / Healthy	19	4
	Yes/ Glaucoma	2	25

(E) CGV with Computed CDR

Confusion Matrix		Predicted Class: No / Healthy	Predicted Class: Yes/ Glaucoma
Actual Class	No / Healthy	15	8
	Yes/ Glaucoma	6	21

Table 8 CCDR comparison results on AFIO dataset of 50 images with ophthalmologists and CGV CDRs

Comparison	Accuracy analysis		
	% Sensitivity	% Specificity	% Accuracy
CGV	77.78	69.57	72.00
ophthalmologist 1	83	65.38	74
ophthalmologist 2	**100.00**	67.70	80
ophthalmologist 3	83.30	80	82
ophthalmologist 4	**92.59**	**82.61**	**88**
average performance	**87.41**	**72.19**	**79.20**

Bold values indicate best results of the proposed systems.

ophthalmologist 3 classifies 25 out of 30 glaucomatous cases correctly giving 83.3% sensitivity, 16 out of 20 normal cases correctly giving 80% specificity, and give 82% accuracy as shown in Tables 7(C) and 8. Also, finally, a comparison result with ophthalmologist 4 classifies 25 out of 27 glaucomatous cases correctly giving 92.59% sensitivity, 19 out of 23 normal cases correctly giving 82.61% specificity, and give 88% accuracy as shown in Tables 7(D) and 8.

The highest sensitivity is obtained by correlating results with ophthalmologist 2. The highlighted portion of the table also reveals that overall better results are obtained when the proposed system is compared with the annotations provided by the most expert ophthalmologist, i.e. ophthalmologist 4. The proposed system has shown results with 78% sensitivity, 65.2% accuracy and 72% specificity on the AFIO dataset when correlated annotated and CCGV values.

To check the system reliability, the proposed system is compared with already developed systems. There is no such comparison available in the literature, as we have used our own local AFIO dataset and there is no benchmark dataset available for glaucoma detection using OCT images publically. Thus, for performance comparison, MATLAB code is reproduced without our three major contributions in the proposed system, i.e. quality assessment, hybrid filtering for denoising, and time effective interpolation technique. For an already developed system simple denoising, thresholding, and Bezier curve fitting techniques are used, as these are already been used by other researchers for the same purpose. Our proposed system shows an increase in all three performance parameters, i.e. accuracy, sensitivity, and specificity. Fig. 17 shows the average accuracy, average sensitivity, and average specificity of both systems.

5 Discussion

Glaucoma is a blindness causing eye disease if not treated in time and weakens the nerve cells that assist in visual recognition. The diameter of the optic cup within the optic disc region is increased

due to the excessive IOP, i.e. the main cause for glaucoma presence and succession. The increment in CDR, i.e. cupping is a widely used feature both clinically and in automated glaucoma diagnostic system. This causes the retina to be affected and also decrease the retinal thickness. For glaucoma diagnosis, CDR is calculated by two commonly used imaging modalities, i.e. OCT and fundus imaging. These two imaging technologies based tools are of great use to identify/monitor retinal tissue structures to treat earlier with ocular diseases. Previously different research studies have CCDR in fundus retinal images by segmenting optic cup and disc regions and then their diameters calculation. This research focuses on the reliable extraction of CDR using OCT, and then classifies the subject as glaucomatous or normal. A new method for extraction of ILM and RPE layers from the OCT scans is developed. The proposed method then used both ILM and RPE for calculation of cup and disc which eventually helps in CDR calculation. Based on the calculated CDRs, the system classifies the patient as normal or glaucomatous. The evaluation is done using a local dataset of 50 OCT scans and results show the validity of the proposed system. The dataset is obtained from AFIO, Pakistan.

6 Conclusion

OCT facilitates in accurate retinal disease diagnosis and retinal recognition and is used to compute this incremented CDR known as cupping in glaucomatic patients. Previous work was mainly focused on the 2D analysis of retina but now the proposed algorithm uses 3D analysis of retina. The proposed system for ILM interpolation is very time effective as it takes 0.0087 s compared to the traditional Bezier curve fitting method for ILM interpolation that takes 9.83 s. This elapsed time shows that the proposed method is 1000 times computational effective as compared to the Bezier curve. Using ILM and RPE layers, the CCDR using the proposed algorithm is then compared with CCGV and clinical values to check the reliability of our CAD system. For clinical correlation, the CCDRs on the whole dataset are compared with annotated CDRs by four ophthalmologists. CDR values ≥ 0.5 are considered glaucomatous, and <0.5 as normal. The proposed system provides a mean error on CCDR when compared with all annotated CDR on the whole 50 datasets to be 0.138 ± 0.026. The proposed system has shown excellent results with 87% sensitivity, 79% accuracy and 72% specificity on the AFIO dataset when correlated annotated and CCGV values. The annotations are provided by the senior doctors. Therefore, the proposed system can be used as a referral system from remote areas to specialists in main cities and promotes the e-health field at the retinal level and the decision-support system by the young doctors.

In future, the proposed system can be further improved by analysing thickness estimation of the OCT retinal layer, i.e. the RNFL that undergoes changes due to the degeneration of ganglion cells in order to diagnose glaucoma before irreversible damage occurs to the optic disc, optic nerve head, and vision. Secondly, the automated algorithm can be created by combining the proposed algorithm with a visual field test.

7 Acknowledgments

This work has been tested on the local dataset and annotations provided by AFIO, Pakistan, and carried out at the Biomedical Image/Signal Analysis (BIOMISA) www.biomisa.org Research Lab, National University of Sciences & Technology, Islamabad, Pakistan. This research is funded by the Higher Education Commission (HEC) Pakistan under grant number 5980/Federal/NRPU/R&D/HEC/2016. Glaucoma analysis using OCT images is also supported by the IGNITE National technology Fund, Pakistan.

8 References

[1] Doi, K.: 'Computer-aided diagnosis in medical imaging: historical review, current status and future potential', *Comput. Med. Imaging Graph.*, 2007, **31**, (4–5), pp. 198–211

[2] 'Medical imaging modalities', 27 November 2017. Available at http://www.medicalimaging.org/about-mita/medical-imaging-primer/

[3] Kondo, T., Ueno, J., Takao, S.: 'Medical image diagnosis of lung cancer by hybrid multi-layered GMDH-type neural network'. Proc. 2012 ICME, Int. Conf. on Complex Medical Engineering, Kobe, Japan, 2012

[4] Thylefors, B., Negrel, A.D.: 'The global impact of glaucoma', *Bull. World Health Organ.*, 1994, **72**, (3), pp. 323–326

[5] Tham, Y.C., Li, X., Wong, T.Y., *et al.*: 'Global prevalence of glaucoma and projections of glaucoma burden through 2040: a systematic review and meta-analysis', *Am. Acad. Ophthalmol.*, 2014, **121**, (11), pp. 2081–2090

[6] Cook, C., Foster, P.: 'Epidemiology of glaucoma: what's new?', *Can. J. Ophthalmol.*, 2012, **47**, (3), pp. 223–226

[7] 'Glaucoma in Asian populations', 27 November 2017. Available at https://www.glaucoma.org/gleams/glaucoma-in-asian-populations.php

[8] Nithya, R., Venkateswaran, N.: 'Analysis of segmentation algorithms in colour fundus and OCT images for glaucoma detection', *Indian J. Sci. Technol.*, 2015, **8**, (24), pp. 1–6

[9] 'Vision Science and Advanced Retinal Imaging (VSRI) Laboratory, University of California, Davis'. Available at http://vsri.ucdavis.edu/research/retinal/oct, accessed 2017

[10] 'Get Familiar with SD-OCT', 2017. Available at https://www.reviewofoptometry.com/ce/get-familiar-with-sd-oct

[11] Hrynchak, P., Hutchings, N., Jone, D., *et al.*: 'A comparison of cup-to-disc ratio measurement in normal subjects using optical coherence tomography image analysis of the optic nerve head and stereo fundus biomicroscopy', *Ophthalmic Physiol. Opt.*, 2004, **24**, (6), pp. 543–550

[12] Usman, M., Fraz, M.M., Barman, S.A.: 'Computer vision techniques applied for diagnostic analysis of retinal OCT images: a review', *Arch. Comput. Methods Eng.*, 2016, **24**, (3), pp. 449–465

[13] Radcliffe, N.M., Hussnain, S.A.: '*Optical coherence tomography in glaucoma*', (Springer, Berlin, 2018)

[14] Lee, J.W., Morales, E., Sharifipour, F., *et al.*: 'The relationship between central visual field sensitivity and macular ganglion cell/inner plexiform layer thickness in glaucoma', *Br. J. Ophthalmol.*, 2017, **101**, (8), pp. 1052–1058

[15] Gondal, T.M., Qazi, Z.U.A., Jamil, A.Z., *et al.*: 'Accuracy of the retinal nerve fiber layer measurements by stratus optical coherence tomography for perimetric glaucoma', *J. Coll. Phys. Surg. Pak.*, 2011, **21**, (12), pp. 749–752

[16] Morgan, J.E., Tribble, J., Fergusson, J., *et al.*: 'The optical detection of retinal ganglion cell damage', *Eye*, 2017, **31**, (2), p. 199

[17] Rao, H.L., Hussain, R.S.M., Januwada, M., *et al.*: 'Structural and functional assessment of macula to diagnose glaucoma', *Eye*, 2016, **31**, (4), pp. 593

[18] Argo, C., Sadiq, M.A., Hassan, M., *et al.*: 'Assessment of change in retinal layers at the Macula in glaucoma patients and correlation to visual field Index'. Investigate Ophthalmology and Visual Science, ARVO Annual Meeting, Seattle, USA, 2016, vol. 57, p. 369

[19] Ahn, J., Yun, I.S., Yoo, H.G., *et al.*: 'Developing new automated alternation flicker using optic disc photography for the detection of glaucoma progression', *Eye*, 2017, **31**, (1), pp. 119–126

[20] Graham, S.L., Bennett, L., Wechsler, D.: 'Patterns of ganglion cell loss, influence of scan area and OCT segmentation strategies in detection of glaucoma', *ARVO Invest. Ophthalmol. Vis. Sci.*, 2016, **57**, p. 849

[21] Hammel, N., Belghith, A., Medeiros, F.A., *et al.*: 'Diagnostic innovations in glaucoma study (DIGS): comparing the rates of macular ganglion cell layer loss in healthy, non-progressing glaucoma and progressing glaucoma eyes', *ARVO, Ophthalmol. Vis. Sci.*, 2016, **57**, p. 373

[22] Wang, Y.-P., Chen, Q., Lu, S.-T.: 'Quantitative assessments of cup-to-disk ratios in spectral domain optical coherence tomography images for glaucoma diagnosis'. Sixth Int. Conf. on in Biomedical Engineering and Informatics (BMEI), Hangzhou, China, 2013

[23] Rajan, A., Ramesh, G.P.: 'Automated early detection of glaucoma in wavelet domain using optical coherence tomography images', *Biosci. Biotechnol. Res. Asia*, 2015, **12**, (3), pp. 2821–2828

[24] Karthik, G., Sivaswamy, J., Mansoori, T.: 'Automatic glaucoma assessment from angio-OCT images'. 2016 IEEE 13th Int. Symp. on Biomedical Imaging (ISBI), Prague, Czech Republic, 2016

[25] Ganesh, T.R., Devib, S.S., Venkatesh, R.: 'Optic nerve head segmentation using fundus images and optical coherence tomography images for glaucoma detection', *Biomed. Pap. Med. Fac. Univ. Palacky*, 2015, **159**, (4), pp. 607–615

[26] Shah, A., Wang, J., Garvin, M.K., *et al.*: 'Automated surface segmentation of internal limiting membrane: spectral-domain optical coherence tomography volumes with a deep cup using A 3-D range expansion approach', China, 2014

[27] Yang, Q., Reisman, C.A., Wang, Z., *et al.*: 'Automated layer segmentation of macular OCT images using dual-scale gradient information', *Opt. Express*, 2010, **18**, (20), p. 21293

[28] Leung, C., Chan, W., Hui, Y., *et al.*: 'Analysis of retinal nerve fiber layer and optic nerve head in glaucoma with different reference plane offsets, using optical coherence tomography', *Invest. Ophthalmol. Visual Sci.*, 2005, **46**, (3), p. 891

[29] Hassan, B., Raja, G.: 'Fully automated assessment of macular edema using optical coherence tomography (OCT) images'. Int. Conf. on Intelligent Systems Engineering (ICISE), Islamabad, Pakistan, 2016

[30] Gonzalez, R.C., Woods, R.E.: 'Digital image processing', (Pearson, Upper Saddle River, 2007, 3rd edn.)

[31] Chaudhury, K.N., Dabhade, S.D.: 'Fast and provably accurate bilateral filtering', *IEEE Trans. Image Process.*, 2016, **25**, (6), pp. 2519–2528

[32] Zhang, Y.J.: '*Image engineering*', vol. **1**, (De Gruyter, Berlin, 2017)

[33] Boomgard, V.D.R., Balen, R.V.: 'Methods for fast morphological image transforms using bitmapped images', *Comput. Vis. Graph. Image Process., Graph. Models Image Process.*, 1992, **54**, (3), pp. 252–254

[34] Adams, R.: 'Radial decomposition of discs and spheres', *Comput. Vis. Graph. Image Process., Graph. Models Image Process.*, 1993, **55**, (5), pp. 325–332

[35] Zneit, R.A., Alqadi, Z.: 'Procedural analysis of RGB color image objects', *Int. J. Comput. Sci. Mob. Comput.*, 2017, **6**, (1), pp. 197–204

[36] Tsai, J.C.: 'How to evaluate the suspicious optic disc', MD New York City, 15 June 2005, accessed 1 December 2017